Materials and Structures (2022) 55:12
https://doi.org/10.1617/s11527-021-01842-3

ORIGINAL ARTICLE

Local Al network and material characterization of belite-calcium sulfoaluminate (CSA) cements

Joonho Seo · Solmoi Park · Seonhyeok Kim · H. N. Yoon · H. K. Lee

Received: 3 December 2020 / Accepted: 6 December 2021 / Published online: 29 December 2021

Abstract The present study investigates the local Al network and material characterization of belite-calcium sulfoaluminate (CSA) cements to provide a comprehensive understanding of the hydration products and characteristics of CSA cements. In this context, the present study elucidates relationships between detailed Al network and microstructural characteristics which can offer an in-depth view of such binder systems. CSA cements having various molar ratios of calcium sulfate to ye'elimite were prepared by controlling the externally incorporated anhydrite dosages. Hydration products of the samples were explored using solid-state ^{27}Al MAS and CPMAS NMR spectroscopy methods and XRD, while MIP and compressive strength tests were used to characterize the samples. The NMR spectroscopy results revealed that the resonance characteristics arising in the tetrahedral Al environment of the samples were identical due to the small potential amounts of C–S–H and strätlingite, whereas Al incorporation in C–S–H was unclear. The MIP analysis showed that the formation of ettringite significantly altered the amount of micropores and mesopores volumes, an outcome which was found to be closely related to the development of compressive strength.

Keywords Belite-calcium sulfoaluminate cement · Anhydrite · Hydration · Characterization · Material design

J. Seo · S. Kim · H. N. Yoon · H. K. Lee (✉)
Department of Civil and Environmental Engineering, Korea Advanced Institute of Science and Technology (KAIST), 291 Daehak-ro, Yuseong-gu, Daejeon 34141, Republic of Korea
e-mail: haengki@kaist.ac.kr

S. Park
Department of Civil Engineering, Pukyong National University, 45 Yongso-ro, Namgu, Busan 48513, Republic of Korea

1 Introduction

Portland cement is the single most widely used construction material in the world, and no alternative cements can sufficiently replace Portland cement on the global scale at present. Consistently pilloried by numerous social institutes and academia, the environmental credentials of Portland cement have been under scrutiny. The manufacturing of Portland cement is responsible for approximately 6–8% of all man-made CO_2 emissions, with an annual production of 4 billion tons [1, 2]. Furthermore, the overall production of Portland cement worldwide has been growing rapidly, posing significant threats to the earth's atmospheric environment [3]. In this regard, increasing demands to devise low-carbon cementing binders have promoted the use of belite-calcium sulfoaluminate (CSA)

cement inasmuch as the production of CSA clinker requires a low calcination temperature of approximately 1250 °C [4], whereas Portland cement clinker is created at a higher calcination temperature of approximately 1450 °C [4–6]. Moreover, the raw materials used to synthesize CSA clinkers can be replaced with various types of industrial waste [7–9].

CSA clinker is primarily composed of ye'elimite and belite, in which the synthesis of these clinkers requires lower $CaCO_3$ input as a raw meal [7], thus addressing the major issues related to the environmental impact of Portland cement production. Since the first discover of ye'elimite-based cement in the 1960s [10], it has been selectively applied for particular purposes over the last several decades due to tailored material behaviors such as rapid setting and shrinkage compensation [11]. These properties are particularly attributed to the hydration of ye'elimite in the presence of calcium sulfate, as expressed in Eqs. (1 and 2), representing the reaction pathway in the absence and presence of portlandite, respectively [12]. Meanwhile, the depletion of gypsum leads to the formation of monosulfate (Eq. 3) [13, 14]. The volumetric calculation on the solids in Eqs. (1 and 3) indicates that 190% and 158% of the volume was increased after full reaction, respectively, indicating that ettringite formation is more preferred in porosity reduction than monosulfate formation. Other than these, strätlingite can slowly form due to the reaction of belite in the absence of portlandite (Eq. 4) [14].

$$C_2A_3S + 2CSH_2 + 36H \rightarrow C_6AS_3H_{32} + 2AH_3 \quad (1)$$

$$C_4A_3S + 8CSH_2 + 6CH + 74H \rightarrow 3C_6AS_3H_{32} \quad (2)$$

$$C_4A_3S + 18H \rightarrow C_4ASH_{12} + 2AH_3 \quad (3)$$

$$C_2S + AH_3 + 5H \rightarrow C_2ASH_8 \quad (4)$$

In the CSA clinker system, ye'elimite and belite phase typically account for of 35–70 and 15–20 wt%, respectively [15–17], while minor phases such as mayenite, brownmillerite and perovskite constitute the remaining portion [15].

As expressed in Eqs. (1–3), which is based on the thermodynamic equilibrium, a deficient supply of calcium sulfate during the hydration of ye'elimite leads to the formation of monosulfate, indicating that the phase assemblage of CSA cements is heavily dependent on the molar ratio of calcium sulfate to ye'elimite (typically referred to as the *m* value). Although controlling the amount of calcium sulfate in the CSA cements can yield ettringite-rich paste [18], this can have unexpected volumetric instability with regard to the long-term durability of the paste [19]. Therefore, without sufficient considerations of the CSA clinker composition and calcium sulfate content, the formation of ettringite in a confined matrix, similar to the phenomenon observed in high-early-strength or rapidly setting cements, may be depreciated to produce an indiscreet expansive paste [20].

Despite that many earlier works have attempted to investigate the hydration kinetics with different calcium sulfate content, detailed elucidations on the Al network and microstructural evolution of CSA cements and their relationships in addition to the hydration characteristics are necessary in order to fully understand such systems. The present study, therefore, provides a comprehensive understanding of the hydration products and material characteristics of CSA cements having various calcium sulfate contents. Commercially available CSA clinker was blended with pure calcium sulfate (anhydrite) to prepare CSA cements. An Al network of the CSA cements was explored with the aid of solid-state ^{27}Al magic angle spinning nuclear magnetic resonance (MAS NMR) and ^{27}Al cross-polarization (CP) MAS NMR techniques, which are highly renowned for demonstrating the Al structures of hydration products in cementitious materials regardless of their crystallinity [21]. The material characteristics of the CSA cements were examined by means of X-ray diffractometry (XRD), compressive strength tests, and mercury intrusion porosimetry (MIP).

2 Experimental program

2.1 Materials and curing condition

CSA clinker and anhydrite powder (anhydrous $CaSO_4$, 99% purity) were used to prepare the CSA cements. XRD pattern and chemical composition of the CSA clinker are provided in Fig. 1 and Table 1, respectively. A quantitative XRD analysis using Rietveld refinement was carried out in order to quantify the mineral composition of the CSA clinker (Table 2). The clinker is mainly composed of ye'elimite and belite with several minor components.

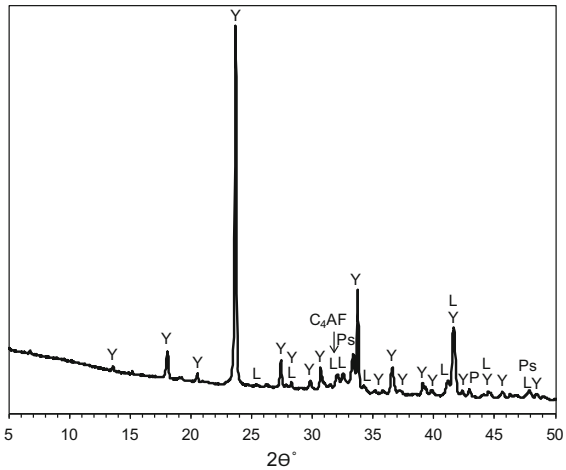

Fig. 1 XRD pattern of belite-calcium sulfoaluminate clinker used in this study. The annotations indicate: Y–ye'elimite, L–β-belite, Ps–perovskite, and C4AF–brownmillerite

respectively. The m value of the samples was determined as the molar ratio of calcium sulfate over ye'elimite and was controlled by the input anhydrite. The *m* values of the samples designed in this study indicate that the samples can be categorized either as rapid-hardening/high-strength (*m* value < 1.5) or as expansive ($1.5 < m$ value < 2.5) [18, 22]. Paste samples were synthesized with a water-to-cement ratio of 0.4. The water-to-cement ratio used in this study was referenced from a previous study in the literature which attempted to use CSA cements in a practical manner [23]. Samples were fabricated using a mechanical mixer for 5 min and were poured into cubical molds with dimensions of $50 \times 50 \times 50$ mm^3. Note that retarder was not adopted in the mixing procedure. The samples were demolded after 1 day of curing and cured in a curing chamber (25 °C). They

Table 1 Chemical composition of belite-calcium sulfoaluminate clinker

Chemical composition (wt%)											
CaO	Al_2O_3	SO_3	SiO_2	MgO	Fe_2O_3	TiO_2	SrO	K_2O	P_2O_5	Na_2O	L.O.I.*
42.97	30.25	9.03	8.41	2.05	1.91	1.42	1.05	0.42	0.167	0.07	2.17

*Loss-on-ignition

Table 2 Mineral composition of belite-calcium sulfoaluminate clinker calculated from quantitative XRD analysis

Mineral	wt%
$C_4A_3\,\overline{S}$ (orthorhombic)	54.1
$C_4A_3\,\overline{S}$ (cubic)	13.4
β-C_2S	18.5
CT	3.5
$C_{12}A_7$	3.4
M	3.2
C_3A	2.3
C_4AF	1.4
$C\,\overline{S}$	0.2

The CSA clinker was replaced with anhydrite at 0, 5, 10 and 20% by weight of the CSA clinker. Sample designation and mixture proportion are tabulated in Table 3. It should be noted that the *m* values of G0, G5, G10 and G20 samples were 0, 0.33, 0.67 and 1.56, were perfectly sealed with plastic wrap throughout the curing period so as not to be influenced by undesirable external conditions (i.e., natural carbonation, evaporation of water and external humidity). On testing days, samples for the chemical analyses were immersed in acetone solution to halt further hydration. Fully dried samples were manually pulverized to pass a 75 μm sieve before the analysis. The immersed samples were placed in a vacuum desiccator to evaporate the liquids so as to eliminate any water present in the samples.

2.2 Test methods

The XRD patterns were obtained using an Empyrean instrument with CuKα radiation at a tube current and generator voltage of 30 mA and 40 kV, respectively. Samples were scanned in the range of 5–45 ° 2θ with a step size of 0.026 ° 2θ and at 2.34 s per step. Solid-state ^{27}Al MAS NMR spectra were recorded at the Larmor frequency of 104.3 MHz. The samples were

Table 3 Mixture proportion of samples expressed as mass ratio

Sample ID	Belite-calcium sulfoaluminate clinker	Anhydrite	Water
G0	1.00	–	0.4
G5	0.95	0.05	0.4
G10	0.90	0.10	0.4
G20	0.80	0.20	0.4

packed inside 4 mm o.d. ZrO_2 rotors under an ambient condition (296.5 K). A pulse width of 1.2 μs and a relaxation delay of 2 s were used. External aqueous $AlCl_3$ was used to calibrate the chemical shift at 0 ppm. The solid-state ^{27}Al CPMAS NMR spectra were acquired using an Avance III HD instrument (9.4 T, Bruker, Germany) operated at 400.3 MHz and 104.3 MHz for ^{1}H and ^{27}Al, respectively. A HX CPMAS probe with a 4 mm o.d. ZrO_2 rotor was used. The spectra were collected with a contact time of 1000 μs, a repetition delay time of 4 s, and a spinning rate of 10 kHz with 1600 scans. The MIP technique was adopted to explore the pore characteristics of the samples. The MIP test was performed using an Autopore IV 9500 V.1.05 porosimeter (manufactured by Micromeritics Corp.) under a maximum pressure of 414 MPa. The compressive strength test was carried out using a universal testing machine with a maximum loading capacity of 2500 kN (manufactured by Instron Corp.). The compressive strength test was performed under a constant loading rate of 0.02 mm/s. Four cubical samples were tested to determine the average compressive strength.

3 Results

3.1 X-ray diffractometry

The XRD patterns of the samples after 14 and 28 days of curing are displayed in Fig. 2. The main reaction products of the samples were ettringite ($Ca_6Al_2(SO_4)_3(OH)_{12}\cdot 26H_2O$, #PDF 00-031-0251) and monosulfate ($Ca_2Al(OH)_6(S_{0.5}O_2(OH_2)_3)$, PDF# 01–083-1289). It is interesting to note that the presence of ettringite was observed even in the G0 sample, which had no external SO_4^- supply. Furthermore, ettringite and monosulfate coexisted in all samples regardless of the anhydrite content and curing age. As expected, the formation of ettringite was promoted as the anhydrite content increased [24]. Meanwhile, a noticeable

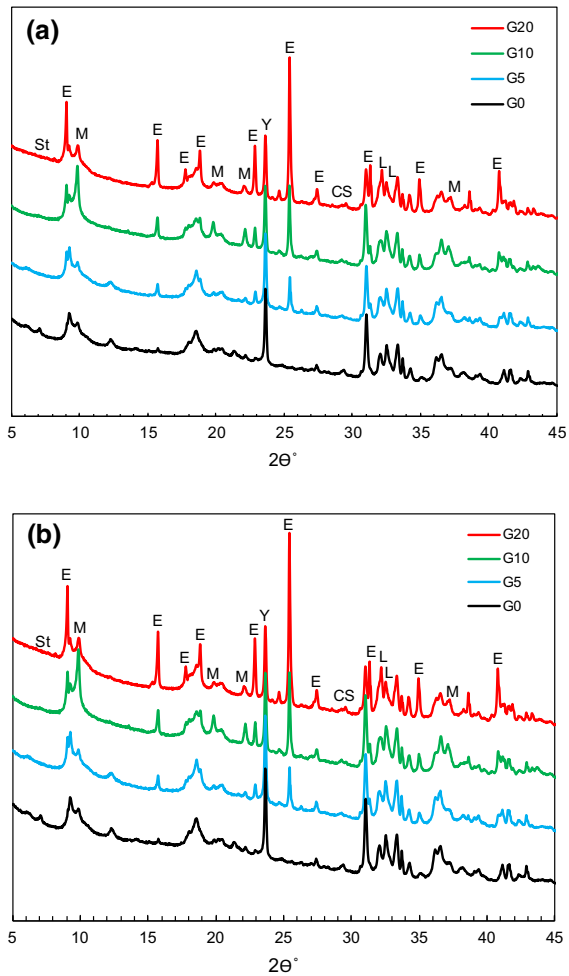

Fig. 2 XRD patterns of samples after (**a**) 14 and (**b**) 28 days of curing. The annotations indicate: Y–ye'elimite, L-β-belite, E–ettringite, St–strātlingite, M–monosulfate and CS-C–S–H

amount of residual crystalline phases, mainly ye'elimite ($Ca_4Al_6(SO_4)O_{12}$, #PDF 00-033-0256) and larnite (β-belite, Ca_2SiO_2, #PDF 00-033-0302), persisted in the samples due to the insufficient curing age and low water-to-cement ratio (i.e., 0.4) [16]. Note that the calculated water-to-cement ratio for the full hydration of CSA clinker increases with an increase in the

anhydrite content (to as high as 0.6 at an anhydrite content of 30 wt%) [4]. Inert clinkers (e.g., CT) [25] were not taken into consideration and are therefore absent in Fig. 2.

Notable differences in the peak intensities in the samples were not observable in the patterns between 14 and 28 days of curing. This implies that the hydration of the samples occurred expeditiously at a very initial curing age. Furthermore, peaks assigned to anhydrite were unidentifiable in all patterns, meaning that the substituted anhydrite was fully consumed. Meanwhile, the hydration of belite was identified by a hump which appeared at 29–30 ° 2θ, which can be assigned to the presence of C–S–H ($Ca_{1.5}SiO_{3.5}H_2O$, #PDF 00-033-0306). A trace of str ā tlingite was observed in the patterns, and its intensity showed inverse proportionality to anhydrite content which is in good agreement with the results reported in the literature [26].

3.2 Solid-state ^{27}Al MAS NMR

The solid-state ^{27}Al MAS NMR spectra of the CSA clinker and the samples after 28 days of curing are shown in Fig. 3. The spectra of the CSA clinker exhibited a broad resonance range throughout the tetrahedral Al region, showing a feature nearly identical to that of synthetic ye'elimite (i.e., two distinctive shoulders at 58 and 68 ppm on the high-field side) [27, 28]. This is attributed to the fact that the contribution of C_4AF does not have any influence on the ^{27}Al MAS NMR spectra owing to ^{27}Al nucleus—Fe^{3+} unpaired electron dipolar couplings and to the

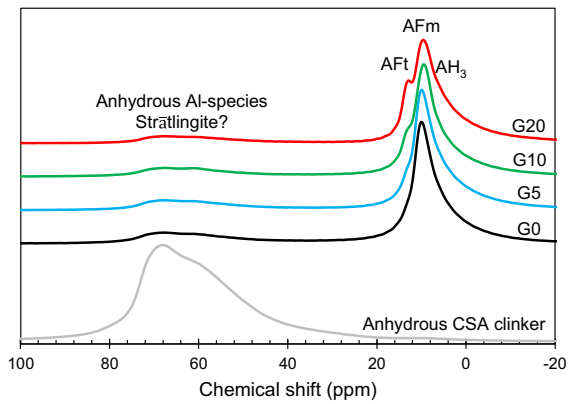

Fig. 3 Solid-state ^{27}Al MAS NMR spectra of belite-calcium sulfoaluminate clinker and samples after 28 days of curing

fact that C_3A scarcely gives rise to resonance [28, 29]. Meanwhile, the hydrated samples showed resonance at 9.5 and 13 ppm, each corresponding to the presence of the AFm and AFt phase at the octahedral sites, respectively [30–33].

An increase in the intensity of the resonance of AFt with an increase in the anhydrite content was confirmed. In addition, as reported in the literature, broad resonance, which partially overlaps with the AFm contribution but is quite distinguishable, is associated with the presence of aluminum hydroxide (AH_3) [34–36]. It is important to note that the resonance of aluminum hydroxide differs from that of third aluminum hydrates, often characterized in the hydration products of Portland cement-based materials and which resonates at around 6–7 ppm [21, 34]. Broad resonance at tetrahedral sites with a constant intensity was observed in all samples. Although one may argue that this resonance is attributed to the presence of tetrahedral Al in C–S–H gels and/or strātlingite [34, 37], the strong overlap with the resonance of ye'elimite does not allow the authors to explain this phenomenon clearly from the ^{27}Al MAS NMR spectra.

In order to resolve the spectral ambiguity featured at the octahedral Al sites and to quantify the hydration products, deconvolution of the spectra was performed with the aid of OriginPro software. Due to the amorphous or poor (disordered) crystallinity characteristics among the CSA cement hydration products (specifically AH_3 and monosulfate) [18], the resonance in these cases is often characterized as an asymmetric peak and can be simulated by a bi-Gaussian function [21, 38]. On the other hand, the Lorentzian function was adopted to simulate the highly symmetric resonance of ettringite at the octahedral Al sites, which exhibit relatively weak quadrupolar effects [34, 39]. Examples of the simulated spectra using the bi-Gaussian function and/or Lorentzian function are presented in Fig. 4. First, the center and width of each peak (the full width half magnitude, FWHM) of the component peaks of the CSA clinker were confirmed. Thereafter, these values were utilized as constraints to simulate the hydrated samples. Note that the deconvolution process was iterated until the estimated chi-square tolerance reached 10^{-9}. A schematic representation of the phase composition based on the deconvolution results is shown in Fig. 5. Deconvolution of the spectra revealed

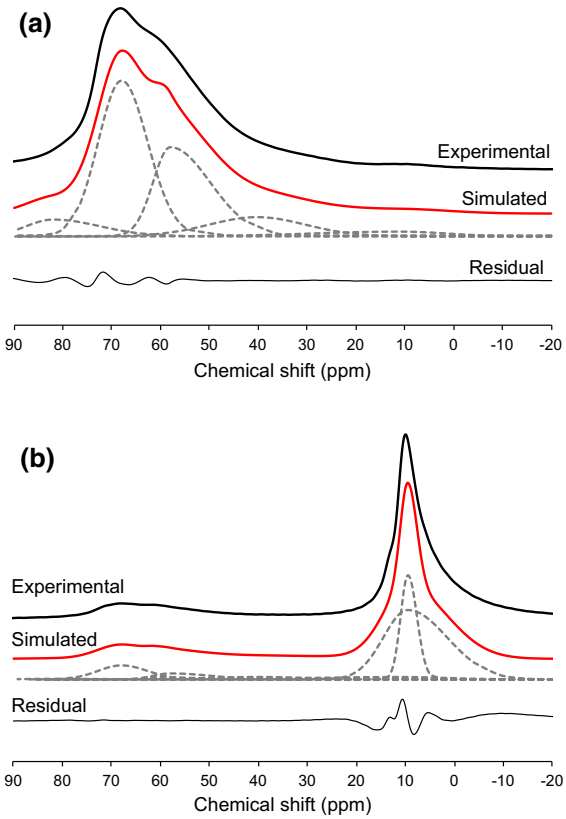

Fig. 4 Examples of simulated solid-state ^{27}Al MAS NMR spectra using bi-Gaussian and/or Lorentzian function. (**a**) belite-calcium sulfoaluminate clinker and (**b**) G5 sample

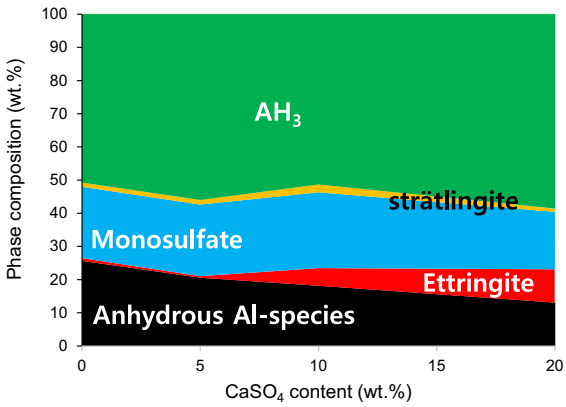

Fig. 5 Schematic representation of phase composition based on the deconvolution results

low and narrow resonance centered at 61 ppm, potentially corresponding to the presence of strätlingite, which is in fair agreement with the line shape and FWHM of the strätlingite contribution as reported in the literature [34, 37]. The relative area of ettringite increased at the expense of monosulfate with an increase in the anhydrite content. The small amount of ettringite was identifiable even in the G0 sample, which is in close agreement with the XRD results. The reduction in the relative area of the anhydrous clinker with an increase in the anhydrite content may be due to the dilution effect of the clinker [40, 41], while the relative areas of AH_3 and strätlingite were unaffected by the anhydrite content.

3.3 Solid-state ^{27}Al CPMAS NMR

The solid-state ^{27}Al CPMAS NMR spectra of the CSA clinker and the samples after 28 days of curing are shown in Fig. 6. The solid-state ^{27}Al CPMAS NMR analysis particularly improves the resonance of Al atoms which are coupled with the water molecules and/or protons of hydroxyl groups [42, 43], signifying that ^{27}Al CPMAS NMR is a useful technique for separating hydrated Al species from anhydrous clinkers. Therefore, the spectra of the CSA clinker showed no Al resonance throughout the obtained spectrum. The spectra of the samples showed an increase in the resonance of AFt with an increase in the anhydrite content. The CPMAS NMR spectra of the hydrated samples showed an increase in the relative intensity of the AFt contribution compared to that observed in the MAS NMR spectra, indicating a higher level of coupling with water molecules and/or hydroxyl groups around Al atoms at 13 ppm [43]. A trace of the AH_3

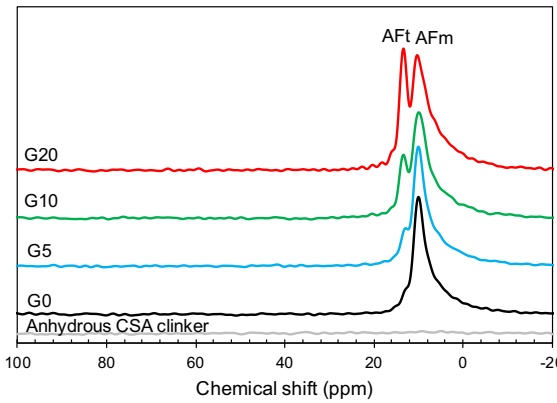

Fig. 6 Solid-state ^{27}Al CPMAS NMR spectra of anhydrous belite-calcium sulfoaluminate clinker and samples after 28 days of curing

contribution, which is considered to be superimposed throughout octahedral Al sites, was more obvious in the CPMAS NMR spectra due to the compelling amount of water bound to a single Al atom and to the prevailing production amount during hydration. Meanwhile, the hydrated samples showed no identifiable signals at the tetrahedral Al sites. It should be noted that CPMAS NMR is less efficient for detecting resonances at tetrahedral Al sites than MAS NMR due to the lower possible number of hydroxyl groups bound with tetrahedrally coordinated Al atoms compared to the number bound with octahedrally coordinated Al atoms [43]. Section 4 comments further on this feature.

3.4 MIP

The cumulative pore volume curves of the samples after 28 days of curing as a function of the pore entry diameter are depicted in Fig. 7a. The samples showed no notable tendency with different anhydrite dosages. The logarithmic derivatives of the cumulative pore volume curves are displayed in Fig. 7b. The G0 and G5 samples showed a prominent pore size distribution in the region of 100–400 nm, while the G10 sample exhibited a representative symptom at the pore region slightly larger than that of G0 and G5 samples. Pores with diameters of 10–100 nm, wich can be assigned to the micropore region, increased particularly in the G20 sample [44, 45]. The magnified pore region of 40,000–400,000 nm is presented in Fig. 7c. The G20 sample showed the lowest pore population in this region. The relative pore volume (%) with respect to total pore volume as classified by a method proposed by Brédy is provided in Table 4 [46]. Clearly, the G20 sample had the highest micropore volume with the lowest mesopore volume. The total porosity, threshold pore diameter, and critical pore diameter of the samples as suggested by Ma [47] are summarized in Table 5. The threshold and critical diameter were smallest in the G20 sample, still the total porosity value was similar regardless of anhydrite content.

3.5 Compressive strength

The compressive strength of the samples after 1, 3, 5, 7, and 28 days of curing are shown in Fig. 8. The compressive strength of the G0, G5, G10 and G20 samples after 1 day of curing were 22.6, 28.8, 32.6 and 36.8 MPa, respectively, showing rapid early strength development proportional to the anhydrite content. The compressive strength of the samples increased continuously with a reduced development rate until 28 days of curing. The compressive strength of the G10 sample after 5 days of curing was measured to be lower than that of the G5 sample, and this reversal in the strength was unaltered until 28 days of curing. The compressive strength of the G0, G5, G10 and G20 samples after 28 days of curing were 37.64, 42.55, 41.05 and 54.11 MPa, respectively.

4 Discussion

The solid-state ^{27}Al MAS NMR results displayed an obvious feature in the tetrahedral Al region, resulting in uncertainty when attempting to elucidate this phenomenon. Explicitly, ^{27}Al CPMAS NMR revealed no resonance in the tetrahedral Al region, indicating the absence of Al-incorporated C–S–H and strätlingite in the samples. However, CPMAS NMR has a certain weakness when used to detect hydration products in this region due to the small number of water molecules bound to the products. In contrast, XRD patterns of the samples revealed the presence of C–S–H and strätlingite. Given that C–S–H is a secondary reaction product of belite after the formation of strätlingite, the amount of C–S–H is inevitably small or its reaction may not have occurred [14, 48]. Under circumstances when the amount of belite is greater than that of ye'elimite or when the *m* value exceeds 2, C–S–H formation is promoted prior to strätlingite formation [14]. In addition, a previous study conducted by Faucon et al. demonstrated that the synthesis of C–S–H with AH_3 does not always lead to the formation of Al-incorporated C–S–H [49], which is possibly associated with the test results from ^{27}Al CPMAS NMR. Recall that the no signals were observed in the tetrahedral Al region of ^{27}Al CPMAS NMR spectra of the samples, indicating the absence of Al-incorporated C–S–H. Therefore, the formation of both C–S–H and strätlingite is likely to occur in the samples used in this study. Nonetheless, it remains necessary to carry out further analyses for a clear identification of the distribution of the hydration products (e.g., SEM–EDS mapping).

Strätlingite generally forms in a clinker system having belite as a minor component [14]. In the CSA-based binder, the formation of strätlingite is promoted

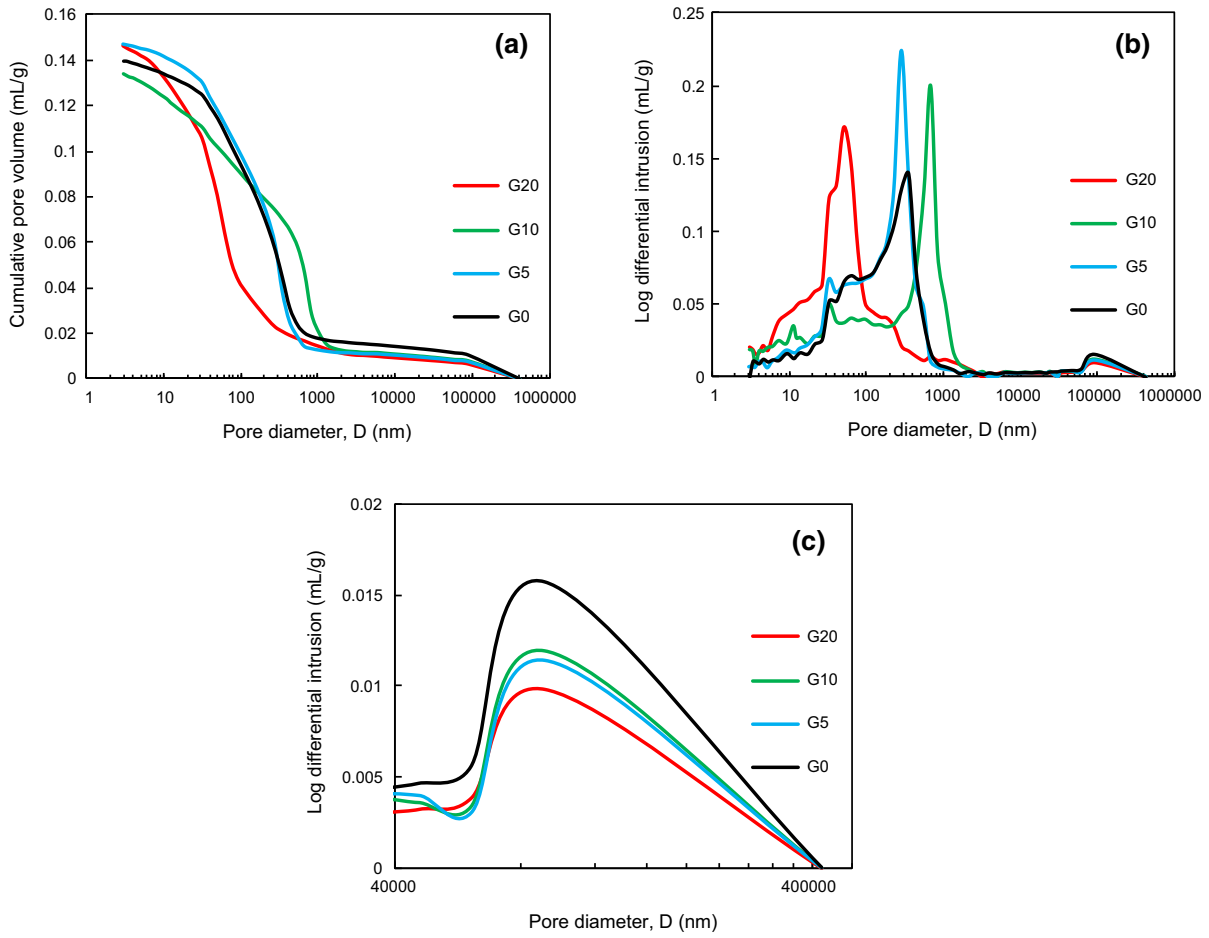

Fig. 7 Mercury intrusion porosimetry test results of samples after 28 days of curing. (**a**) Cumulative pore volume curves, (**b**) their first derivatives, and (**c**) magnification of (b) in the region of 40,000–400,000 nm

Table 4 The relative pore volume of micropore and mesopore region with respect to total pore volume

Sample ID	Micropore (%)	Mesopore (%)
G0	36.59	48.99
G5	36.41	53.80
G10	35.00	30.23
G20	74.19	14.35

by the hydration of belite with the consumption of AH_3 only in the absence of portlandite (Eq. 4). The absence of portlandite was evidenced by the XRD results, meaning that a preferable condition for strätlingite formation existed. In particular, at around 5–7 days of curing, when belite starts to take part in the reaction, the hydration of belite accompanies the formation of strätlingite, which fills the voids of the inner matrix, creating a very dense structure [34]. As revealed via the XRD patterns, the amount of strätlingite produced was inverse proportional to the anhydrite content, which is in close agreement with the fact that the Al concentration in the pore solution decreases when sulfate ions are depleted to form strätlingite. Considering that the compressive strength increase due to ettringite formation occurs at an early age and that the reversal of the compressive strength of the G5 and G10 samples remained unchanged until 28 days of curing, the formation of strätlingite partially contributed to the development of compressive strength after five days of curing, when belite started to react with AH_3. Note that a similar observation was reported in a previous study,

Table 5 The pore parameters of the samples

Sample ID	Total porosity (%)	Threshold pore diameter (nm)	Critical pore diameter (nm)
G0	24.04	505	320
G5	25.01	380	280
G10	23.07	1060	670
G20	24.78	82	51

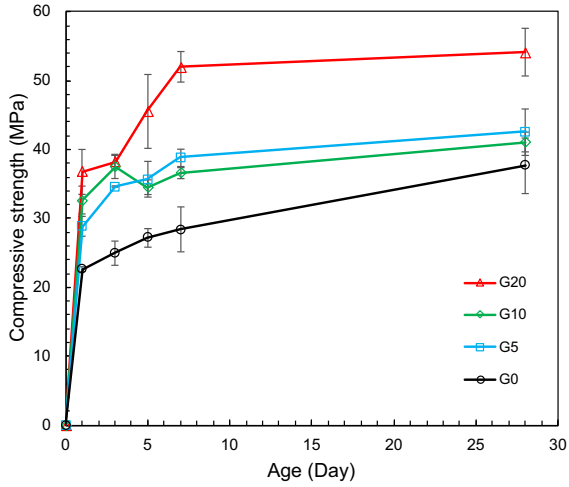

Fig. 8 Compressive strength development of the samples

demonstrating that no correlation between the *m* value and the compressive strength of CSA cement mortar cube was identified for specimens having *m* values between 0 and 1 [26].

The relationship between the relative micropore or mesopore volume and ettringite formation, each estimated by the MIP test results and deconvolution of the ^{27}Al MAS NMR spectra, respectively, is plotted in Fig. 9. Apparently, an increase in the amount of ettringite increased the micropore volume, and vice versa with regard to mesopore volume, which in turn significantly affected the development of compressive strength in the samples. Thus, the decrease in the mesopore volume due to the formation of ettringite resulted in high compressive strength. It should be noted that the total amount of the AFm and AFt phases (wt. %) is always identical even with different *m* values due to the Al balance [26]. On the other hand, as unveiled in the results presented here, the presence of ettringite was observed even in the G0 sample. As postulated in the literature, the hydration of pure ye'elimite can produce ettringite without external SO_4^{-2} sources, as expressed in Eq. (5) [18, 50], which may partially contribute to the rapid development of compressive strength in the G0 sample at an early age. However, the presence of C_3AH_6 (katoite) was unidentifiable in the XRD patterns inasmuch as the amount of C_3AH_6 was below the detection limit [18].

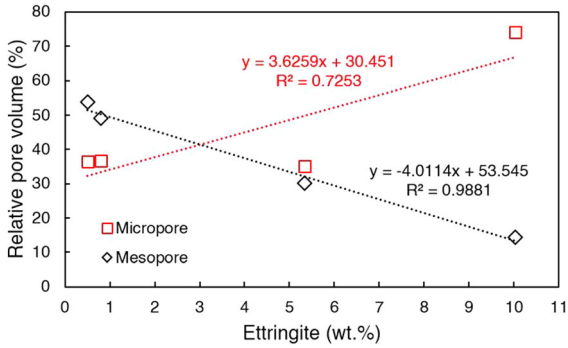

Fig. 9 Relationship between relative micropore or mesopore volume and ettringite formation

$$C_4A_3S + 80H \rightarrow C_6AS_3H_{32} + C_4ASH_{12} + 2C_3AH_6 + 8AH_3 \quad (5)$$

5 Conclusion

The present study investigated the local Al environment and undertook a material characterization of CSA cements and presented the material characteristics of the CSA cements. The hydration properties of CSA cements having various *m* values were explored by solid-state ^{27}Al MAS and CPMAS NMR spectroscopy methods, by XRD and MIP analyses, and by compressive strength tests. The results obtained in this study revealed that externally incorporated anhydrite significantly altered the composition of the hydration products and pore characteristics, which are ultimately responsible for mechanical strength and durability. The primary outcomes gleaned from this study are listed below.

(1) XRD and ^{27}Al MAS and CPMAS NMR spectroscopy outcomes demonstrated the presence of C–S–H and strätlingite, though the amounts of these materials are inevitably small and Al substitution within C–S–H is unclear.
(2) Samples having *m* values of less than 2 (i.e., deficient ettringite formation) showed a reversal of the compressive strength with an increase in the anhydrite content shortly after belite took part in the reaction, forming strätlingite.
(3) The formation of ettringite led to the evolution of the micropore volume while decreasing the mesopore volume, resulting in the development of compressive strength throughout the curing period.

Acknowledgements This study was supported by the National Research Foundation of Korea (NRF) funded by the Korean government (Ministry of Science & ICT) [Grant Number: 2017R1A5A1014883] through Smart Submerged Floating Tunnel System Research Center. The authors acknowledge the use of solid-state NMR spectrometer at Korea Basic Science Institute Western Seoul center, and would like to thank Dr. Seen-Ae Chae for assistance with NMR spectroscopy.

Funding The participation of Joonho Seo, Solmoi Park, Seonhyeok Kim, H.N. Yoon, and H.K. Lee was sponsored by the NRF funded by the Korean government.

Declarations

Conflict of interest The authors declare that they have no conflict of interest and have agreed the submission of the manuscript.

References

1. Ayer NW, Dias G (2018) Supplying renewable energy for Canadian cement production: life cycle assessment of bioenergy from forest harvest residues using mobile fast pyrolysis units. J Clean Prod 175:237–250
2. Pedersen MT, Jensen F, Skibsted J (2018) Structural investigation of ye'elimite, $Ca_4Al_6O_{12}SO_4$, by ^{27}Al MAS and MQMAS NMR at different magnetic fields. J Phys Chem C 122:12077–12089
3. Andrew RM (2018) Global CO_2 emissions from cement production. Earth Sys Sci Data 10:195
4. Glasser FP, Zhang L (2001) High-performance cement matrices based on calcium sulfoaluminate-belite compositions. Cem Concr Res 31:1881–1886
5. Hargis CW, Telesca A, Monteiro PJM (2014) Calcium sulfoaluminate (Ye'elimite) hydration in the presence of gypsum, calcite and vaterite. Cem Concr Res 65:15–20
6. Taylor HFW (1997) Cement chemistry. London, UK, Thomas Telford
7. Chen IA, Juenger MCG (2012) Incorporation of coal combustion residuals into calcium sulfoaluminate-belite cement clinkers. Cem Concr Compos 34:893–902
8. Sahu S, Majing J (1994) Preparation of sulphoaluminate belite cement from fly ash. Cem Concr Res 24:1065–1072
9. Beretka J, De Vito B, Santoro L, Sherman N, Valenti GL (1993) Hydraulic behaviour calcium sulfoaluminate-based cements derived from industrial process wastes. Cem Concr Res 23:1205–1214
10. Klein A (1963) Calciumaluminosulfate and expansive cements containing same, US Patent No. 3:155, 526, 4
11. Bizzozero J, Gosselin C, Scrivener KL (2014) Expansion mechanisms in calcium aluminate and sulfoaluminate systems with calcium sulfate. Cem Concr Res 56:190–202
12. Older I (2000) Cements containing calcium sulfoaluminate. In: Special Inorganic cements; Bentur A, Mindess S (Eds.) E & FN Spon: London, UK, 69–87
13. García-Maté M, Angeles G, León-Reina L, Losilla ER, Aranda MA, Santacruz I (2015) Effect of calcium sulfate source on the hydration of calcium sulfoaluminate eco-cement. Cem Concr Compos 55:53–61
14. Winnefeld F, Lothenbach B (2010) Hydration of calcium sulfoaluminate cement – experimental findings and thermodynamic modelling. Cem Concr Res 40:1239–1247
15. Factsheet MP (2014) Mineral planning factsheet, Available online: https://www.bgs.ac.uk/downloads/start.cfm?id=1353 (accessed on 14 November 2018)
16. Jeong Y, Hargis C, Chun S, Moon J (2017) Effect of calcium carbonate fineness on calcium sulfoaluminate-belite cement. Mater 10:990
17. Bernardo G, Telesca A, Valenti GL (2006) A porosimetric study of calcium sulfoaluminate cement pastes cured at early ages. Cem Concr Res 36:1042–1047
18. Winnefeld F, Barlag S (2009) Calorimetric and thermogravimetric study on the influence of calcium sulfate on the hydration ye'elimite. J Therm Anal Calorim 101:949–957
19. Liu Z, Li X, Deng D, De Schutter G (2016) The damage of calcium sulfoaluminate cement paste partially immersed in MgSO4 solution. Mater Struct 49:719–727
20. Beltagui H, Jen G, Whittaker M, Imbabi MS (2017) The influence of variable gypsum and water content on the strength and hydration of a belite-calcium sulphoaluminate cement. Adv Appl Ceram 116:199–206
21. Andersen MD, Jakobsen HJ, Skibsted J (2006) A new aluminum-hydrate species in hydrated Portland cements characterized by ^{27}Al and ^{29}Si MAS NMR spectroscopy. Cem Concr Res 36:3–17
22. Zhang L (2000) Microstructure and performance of calcium sulfoaluminate cements, Ph. D. dissertation, University of Aberdeen
23. Luz CA, Rocha JC, Cheriaf M, Pera J (2006) Use of sulfoaluminate cement and bottom ash in the solidification/stabilization of galvanic sludge. J Hazard Mater 136:837–845
24. Telesca A, Marroccoli M, Pace ML, Tomasulo M, Valenti GL, Monteiro PJM (2014) A hydration study of various calcium sulfoaluminate cements. Cem Concr Compos 53:224–232

25. Hargis CW, Lothenbach B, Müller CJ, Winnefeld F (2017) Carbonation of calcium sulfoaluminate mortars. Cem Concr Compos 80:123–134
26. Jen G, Stompinis N, Jones R (2017) Chloride ingress in a belite-calcium sulfoaluminate cement materix. Cem Concr Res 98:130–135
27. Calos NJ, Kennard CH, Whittaker AK, Davis RL (1995) Structure of calcium aluminate sulfate $Ca_4Al_6O_{16}S$. J Solid State Chem 119:1–7
28. Le Saoût G, Lothenbach B, Hori A, Higuchi T, Winnefeld F (2013) Hydration of Portland cement with additions of calcium sulfoaluminates. Cem Concr Res 43:81–94
29. Skibsted J, Jakobsen HJ, Hall C (1998) Quantitative aspects of 27Al MAS NMR of calcium aluminoferrites, 7:57–59
30. Park SM, Jang JG, Lee NK, Lee HK (2016) Physicochemical properties of binder gel in alkali-activated fly ash/slag exposed to high temperatures. Cem Concr Res 89:72–79
31. Park SM, Seo JH, Lee HK (2018) Binder chemistry of sodium carbonate-activated CFBC fly ash. Mater Struct 51:1–10
32. Ke X, Bernal SA, Provis JL (2016) Controlling the reaction kinetics of sodium carbonate-activated slag cements using calcined layered double hydroxides. Cem Concr Res 81:24–37
33. Seo JH, Park SM, Lee HK (2018) Evolution of the binder gel in carbonation-cured Portland cement in an acidic medium. Cem Concr Res 109:81–89
34. Paul G, Boccaleri E, Buzzi L, Canonico F, Gastaldi D (2015) Friedel's salt formation in sulfoaluminate cement: a combined XRD and ^{27}Al MAS NMR study. Cem Concr Res 67:93–102
35. Isobe T, Watanabe T, De La Caillerie JBDE, Legrand AP, Massiot D (2003) Solid-state ^{1}H and ^{27}Al NMR studies of amorphous aluminum hydroxides. J Coll Interf Sci 261:320–324
36. Sánchez-Herrero MJ, Fernández-Jiménez A, Palomo A (2012) Alkaline hydration of tricalcium aluminate. J Am Ceram Soc 95:3317–3324
37. Kwan S, LaRosa J, Grutzeck MW (1995) ^{29}Si and ^{27}Al MASNMR study of stratlingite. J Am Ceram Soc 78:1921–1926
38. Skibsted J, Jakobsen HJ, Hall C (1994) Direct observation of aluminium guest ions in the silicate phases of cement minerals by 27Al MAS NMR spectroscopy. J Chem Soc 90:2095–2098
39. de Lacaillerie JBDE, Fretigny C, Massiot D (2008) MAS NMR spectra of quadrupolar nuclei in diordered solids: the Czjzek model. J Magn Reson 192:244–251
40. Frıas M, De Rojas MIS, Cabrera J (2000) The effect of the pozzolanic reaction of metakolin has on the heat evolution in metakolin-cement mortars. Cem Concr Res 30:209–216
41. Seo JH, Amr IT, Park SM, Bamagain RA, Fadhel BA, Kim GM, Hunaidy AS, Lee HK (2018) CO_2 uptake of carboantion-cured cement blended with ground volcanic ash. Materials 11:2187
42. Schneider J, Cincotto MA, Panepucci H (2001) ^{29}Si and ^{27}Al high-resolution NMR characterization of calcium silicate hydrate phases in activated blast-furnace slag pastes. Cem Concr Res 31:993–1001
43. Zhang W, Ma D, Han X, Liu X, Bao X, Guo X, Wang X (1999) Methane dehydro-aromatization over Mo/HZSM-5 in the absence of oxygen: a multinuclear solid-state NMR study of the interaction between supported Mo species and HZSM-5 zeolite with different crystal sizes. J Catal 188:393–402
44. Jang JG, Lee HK (2016) Microstructural densification and CO_2 uptake promoted by the carbonation curing of belite-rich Portland cement. Cem Concr Res 82:50–57
45. Ambroise J, Georgin JF, Peysson S, Péra J (2009) Influence of polyether polyol on the hydration and engineering properties of calcium sulfoaluminate cement. Cem Concr Compos 31:474–782
46. Bredy P (1990) Etude de la microstructure des liants pouzzolaniques de synthèse. Utilisation de la porosimétrie, Ph. D. Thesis, Lyon, INSA Lyon
47. Ma H (2014) Mercury intrusion porosimetry in concrete technology: tips in measurement, pore structure parameter acquisition and application. J Porous Mater 21:207–215
48. Li GS, Walenta G, Gartner EM (2007) Formation and hydration of low-CO2 cements based on belite, calcium sulfoaluminate and calcium aluminoferrite. In: Proceedings of the 12th ICCC, Montreal, Canada 9–12
49. Faucon P, Charpentier T, Nonat A, Petit JC (1998) Triple-quantum two-dimensional 27Al magic angle nuclear magnetic resonance study of the aluminum incorporation in calcium silicate hydrates. J Am Chem Soc 120:12075–12082
50. Wadsö L (2005) Applications of an eight-channel isothermal conduction calorimeter for cement hydration studies. Cem Int 5:94–101